

Seismic interferometry applied to regional and teleseismic events recorded at Planchón-Peteroa Volcanic Complex, Argentina-Chile

Casas, José Augusto; Badi, Gabriela Alejandra ; Franco, Luis; Draganov, Deyan

DOI

[10.1016/j.jvolgeores.2020.106805](https://doi.org/10.1016/j.jvolgeores.2020.106805)

Publication date

2020

Document Version

Accepted author manuscript

Published in

Journal of Volcanology and Geothermal Research

Citation (APA)

Casas, J. A., Badi, G. A., Franco, L., & Draganov, D. (2020). Seismic interferometry applied to regional and teleseismic events recorded at Planchón-Peteroa Volcanic Complex, Argentina-Chile. *Journal of Volcanology and Geothermal Research*, 393, 1-10. Article 106805.
<https://doi.org/10.1016/j.jvolgeores.2020.106805>

Important note

To cite this publication, please use the final published version (if applicable).
Please check the document version above.

Copyright

Other than for strictly personal use, it is not permitted to download, forward or distribute the text or part of it, without the consent of the author(s) and/or copyright holder(s), unless the work is under an open content license such as Creative Commons.

Takedown policy

Please contact us and provide details if you believe this document breaches copyrights.
We will remove access to the work immediately and investigate your claim.

Seismic interferometry applied to regional and teleseismic events recorded at Planchón-Peteroa Volcanic Complex, Argentina-Chile

Casas, José Augusto^a, Badi, Gabriela Alejandra^b, Franco, Luis^c, Draganov, Deyan^d

^a*Facultad de Ciencias Astronómicas y Geofísicas, Universidad Nacional de La Plata, CONICET, Argentina*

^b*Facultad de Ciencias Astronómicas y Geofísicas, Universidad Nacional de La Plata, Argentina*

^c*Observatorio Volcanológico de los Andes del Sur (OVDAS-SERNAGEOMIN), Chile*

^d*Department of Geoscience and Engineering, Delft University of Technology, The Netherlands*

Abstract

The Planchón-Peteroa Volcanic Complex (PPVC) is located in the Central Andes, Argentina-Chile. Even though this active volcanic system is considered one of the most dangerous volcanoes in the region, with more than twenty modest ($VEI < 4$) Holocene eruptions, knowledge of its subsurface structures, internal processes, dynamics, and their relation, is still limited.

Seismic interferometry (SI) is a high-resolution technique based on analyses of the interference of the propagation seismic energy at one or many stations. SI can be used to characterize the subsurface properties of a target area. In particular, previous SI studies performed in the area of the PPVC describe specific ranges of depth; therefore, more information is required for a thorough description of the subsurface features in the area and for a better understanding of the PPVC dynamics.

Email address: acasas@fcaglp.unlp.edu.ar (Casas, José Augusto)

Preprint submitted to Journal of Volcanology and Geothermal Research January 29, 2020

57
58
59
60
61
62
63
64 We apply SI based on autocorrelations of selected regional and tele-
65 seismic events to image the subsurface structures below stations located in
66 Argentina and Chile during 2012. The selection of the events is performed
67 according to their location, magnitude, angle of incidence of P-wave seismic
68 energy, and signal-to-noise ratio in the records. For each station, we extract
69 time windows and we process them using two ranges of frequency, which are
70 sensitive to different depth ranges.
71
72
73

74
75 This work describes depths and zones previously not analyzed in the area
76 using SI methods. The results not only complement the available geological,
77 geochemical, and geophysical information, but present new information for
78 depths between 10 and ~ 750 km depth, increasing the general knowledge of
79 the subsurface features in the PPVC. Finally, we also propose a model for
80 the subsurface down to the Moho, which indicates the crustal structure and
81 the likely distribution of magma bodies in depth.
82
83
84

85 *Keywords:*

86
87 Planchón-Peteroa Volcanic Complex, Seismic Interferometry, Regional and
88 teleseismic events, Magma storage in depth
89
90

91 **1. Introduction**

92
93 The Planchón-Peteroa Volcanic Complex -PPVC- (35.223° S, 70.568° W;
94 see location in [Figure 1](#)) is located in the Andes at the international border
95 between Argentina and Chile. The PPVC is composed of three main volcanic
96 edifices, i.e., the Azufre, the Planchón, and the Peteroa, out of which the
97 latter is the current active volcano. The PPVC presents overlapped calderas
98 originating from the destruction of several volcanic structures during past
99 explosive events ([Tormey, 1989](#)). Through analyses of its historical activity
100 and products, this volcanic system is ranked as the most hazardous volcano
101
102
103
104
105
106

113
114
115
116
117
118
119
120 in Argentina (Elissondo and Farías, 2016) and the eighth most risky volcano
121 in Chile (Technical sheet, Observatorio Volcanológico de los Andes del Sur,
122 OVDAS-SERNAGEOMIN, Chile).

123 The knowledge of the PPVC has been developed by the contribution
124 from several disciplines, i.e., geology (Tormey, 1989; Haller et al., 1994;
125 Naranjo et al., 1999; Tapia Silva, 2010; Haller and Risso, 2011), geochem-
126 istry (Benavente, 2010; Tassi et al., 2016; Benavente et al., 2016), meteorol-
127 ogy (Guzmán et al., 2013), ash analysis (Ramires et al., 2013), seismology
128 (Casas et al., 2014; Manassero et al., 2014; Olivera Craig, 2017; Casas et al.,
129 2018, 2019), gravimetry (Tassara et al., 2006), and risk analysis (Haller and
130 Coscarella, 2011). These studies contribute to the knowledge of the eruptive
131 history and the current subsurface conditions of this volcanic system. Nev-
132 ertheless, the dynamics of the PPVC and their relation with the subsurface
133 structures are still poorly understood, increasing the local risk (Elissondo
134 and Farías, 2016).

135 A description of the subsurface structures (i.e., depth, associated dimen-
136 sions, density contrasts, etc.) is essential for developing accurate knowl-
137 edge of the dynamics of any volcanic system. In particular, knowledge of
138 subsurface discontinuities provides constraints for tomographic studies, for
139 magma-ascent modeling, among others, contributing to a better inference
140 of the subsurface conditions, and, therefore, leading to more reliable analy-
141 ses of likely future volcanic scenarios. Based on structural-geology analyses,
142 Tapia Silva (2010) describes the subsurface geological units located in the
143 very first 10 km of the subsurface in the area of the PPVC, and presents
144 their distribution in depth. Even though no local studies have been applied
145 for describing the crustal structure in the PPVC, Farías et al. (2010) and
146 Giambiagi et al. (2012) provide a crustal structure as a function of depth

169
170
171
172
173
174
175
176 and the distance from the trench in the Central Andes. They indicate the
177
178 crust to be structured by four zones delimited in depth at ~ 12 (upper-crust
179
180 discontinuity), ~ 20 (upper-lower crust discontinuity), and ~ 35 (lower-crust
181
182 discontinuity) km, with uncertainties smaller than 5 km. The crust-mantle
183
184 discontinuity (the Moho) is estimated at ~ 48 km depth, the lithosphere-
185
186 asthenosphere boundary at ~ 75 km depth, and the top of the subducting
187
188 slab (oceanic lithosphere) at ~ 120 km depth (see also [Tassara et al. \(2006\)](#)).
189
190 Nevertheless, more scientific evidence is required to increase the information
191
192 about the known subsurface structures, leading to a more accurate charac-
193
194 terization of their properties, as well as to describe the subsurface features
195
196 previously not analyzed. These goals motivate local studies, as the one
197
198 presented in this article.

199
200
201
202
203
204
205
206
207
208
209
210
211
212
213
214
215
216
217
218
219
220
221
222
223
224
[Claerbout \(1968\)](#) has constituted a frame over which the theory of seis-
mic interferometry developed. This passive seismic method -from here on,
Seismic Interferometry by Autocorrelations (SIbyA)- suggests that the au-
tocorrelation of a plane-wave transmission response propagating in a hori-
zontally layered medium, recorded at the surface, allows the retrieval of the
reflection response of a virtual source co-located with the recording station.
SIbyA has shown to be a robust method; it has been applied to different
types of seismic data, in several areas and at different scales. For example,
SIbyA was applied to global- and teleseismic phases to image the subsurface
at regional scales -array lengths greater than 50 km ([Ruigrok and Wapenaar,](#)
[2012](#); [Nishitsuji et al., 2016](#)), to P-wave of microseismic events to image the
shallow (down to ~ 3 km depth) volcanic subsurface ([Kim et al., 2017](#)), and
to ambient-noise seismic data at several scales -local and regional ([Draganov](#)
[et al., 2007](#); [Gorbatov et al., 2013](#); [Boullenger et al., 2014](#); [Oren and Nowack,](#)
[2017](#); [Delph et al., 2019](#)). The robustness of SIbyA has motivated its ap-

225
226
227
228
229
230
231
232 plication to local (Casas et al., 2019), regional, and teleseismic seismic data
233 (present article) recorded in the area of the PPVC.
234

235 Nishitsuji et al. (2016) apply SIbyA to global seismic phases recorded
236 in the eastern flank of the Peteroa volcano during 2012. They confirm the
237 location of the Moho at ~ 45 -50 km depth, and propose a deformation feature
238 in the subducting slab in the form of detachment, shearing, necking, or any
239 combination of them.
240
241

242 Casas et al. (2019) apply SIbyA to local seismic events to image the sub-
243 surface below the stations located in the Argentine and Chilean sides of the
244 PPVC during 2012. They confirm the geological structure described for the
245 first 4 km of the subsurface (Tapia Silva, 2010), provide information about
246 regions of higher heterogeneity caused by faulting and complex geochemical
247 processes, and support the presence of a magma body emplaced at ~ 4 km
248 depth (previously suggested by Benavente (2010)).
249
250
251
252
253

254 We apply SIbyA to regional and teleseismic events selected according to
255 their location, magnitude, angles of incidence of the P-wave seismic energy
256 at each station, and the signal-to-noise ratio in the records. The results
257 for two different frequency ranges allow the description of the subsurface
258 structures between ~ 10 and ~ 750 km depth, as well as the inference of the
259 crustal structure and the likely location of magma bodies down to the Moho.
260
261
262
263

264 **2. Data**

265
266
267 The present application uses seismic data recorded by stations deployed
268 in Argentina and Chile during 2012 (see station distribution in Figure 1).
269

270 The temporary deployment of seismic instruments in an area of interest
271 is a widely used tool for reaching several goals, e.g., perform first analyses
272
273

281
282
283
284
285
286
287
288 of the propagating wavefield and the subsurface conditions, increase the
289 number of the recording stations, extend the analyzed area, and improve
290 the accuracy of previous results. The MalARRgue project ([Ruigrok et al.,](#)
291 [2012](#)) was designed by institutions from The Netherlands (Delft University
292 of Technology -TUDelft), Argentina (Comisión Nacional de Energía Atómica
293 CNEA), and The United States (Boise State University -BSU). Its goal was
294 imaging and monitoring the subsurface of the Malargüe region (Mendoza,
295 Argentina), an area of high scientific interest due to peculiar volcanic and
296 tectonic processes ([Stern, 2004](#)). The MalARRgue project consisted of a
297 temporal deployment (from January 2012 to January 2013) of 38 stations,
298 out of which six were deployed along the eastern flank of the PPVC (from
299 here on, the PV array). The PV array was equipped with short-period (2
300 Hz) three-component (Sercel L-22) sensors.
301
302
303
304
305
306
307

308 Another source of data is provided by three broad-band stations of the
309 Observatorio Volcanológico de los Andes del Sur (OVDAS-SERNAGEOMIN,
310 Chile), which are located ~ 6 km northwards. These stations (from here on,
311 OVDAS array) were active during 2012, through the same period as the PV
312 array.
313
314
315
316

317 **3. Application and results**

318
319 SIbyA is described by the reciprocity theorem of correlation type ([Wapenaar,](#)
320 [2003, 2004](#)). Based on this theorem for transient sources ([Wapenaar](#)
321 [and Fokkema, 2006](#)), and using autocorrelation in the time domain, we ob-
322 tain:
323
324
325
326
327
328
329
330
331
332
333
334
335
336

$$\begin{aligned}
& \sum_{sources} \{ [T(\mathbf{x}_A, -t) * s_i(-t) * T(\mathbf{x}_A, t) * s_i(t)] \otimes [s(-t) * s(t)]_i \} \\
& \approx -R(\mathbf{x}_A, -t) + \delta(t) - R(\mathbf{x}_A, t) \quad , \quad (1)
\end{aligned}$$

112 which states that the reflection response $R(\mathbf{x}_A, t)$ can be retrieved at
113 the station A located (at \mathbf{x}_A) at the surface through the autocorrelation
114 of a recorded transmitted wavefield $T(\mathbf{x}_A, t)$. The operator $*$ indicates
115 convolution, \otimes means deconvolution, and δ is the Dirac's delta. The fac-
116 tor $[s(-t) * s(t)]_i$ corresponds to the autocorrelated source time function
117 (ASTF), which allows the deconvolution of each source time function $s_i(t)$.

118 Even though [Equation 1](#) requires sources over the whole stationary phase
119 area (i.e., the Fresnel Zone), seismic events present a non-uniform spatial
120 distribution. Therefore, performing a selection of the seismic sources to be
121 used is essential for a proper application of SIbyA. In order the transmission
122 response of the propagating seismic energy to be accurately estimated by
123 the vertical component of the records, we select only seismic events with
124 P-wave seismic energy arriving (sub) vertically to a station at the surface.
125 The retrieved reflection response (from here on, $R_v(\mathbf{x}_A, t)$) is related to a
126 seismic source co-located with the station at the surface, radiating P-wave
127 energy (sub)vertically downwards.

128 A seismic source in the subsurface releases energy that propagates to-
129 wards the surface, where the energy is reflected back to the subsurface. This
130 seismic energy is reflected, refracted, converted and diffracted at the sub-
131 surface structures and heterogeneities (or the surface), part of which arrives
132 to the recording station at the surface. Seismograms are then composed
133 of direct waves followed by these reverberated waves. SIbyA removes the

393
394
395
396
397
398
399
400 times previous to the direct arrival, and attenuates the incoherent noise,
401 providing reflection evidence of the location of the subsurface structures.
402 [Figure 2a](#) depicts the application of SIbyA in an idealized horizontally lay-
403 ered 2-D medium, given a plane wavefield originated by a seismic source
404 located exactly below the station. The obtained virtual reflection response
405 can be used to estimate the depth of the reflectors located in the subsurface
406 below the station. Based on [Nishitsuji et al. \(2016\)](#), [Figure 2b](#) shows the
407 scenarios (except the one shown in [Figure 2a](#)) in which this methodology
408 would (would not) retrieve seismic reflection energy: a gently dipping layer,
409 a steep layer, a stair-like steep layer, and a steep layer with an abrupt break
410 along its structure.
411

412
413
414
415
416
417 In the real Earth, neither the wave fronts are planar at local and regional
418 scales nor is usually the subsurface horizontally layered. In highly hetero-
419 geneous zones (as, for example, the area of the PPVC; [Manassero et al.](#)
420 [\(2014\)](#)), the location of a seismic source exactly below the station is not an
421 imperative condition for an accurate retrieval of the subsurface reflection
422 response $R_v(\mathbf{x}_A, t)$ as small variations in the location of the sources do not
423 affect the propagation of the seismic energy in the area of interest ([Fan and](#)
424 [Snieder, 2009](#)), i.e., the vertical component of the records is still an accu-
425 rate estimation of the transmission response. Therefore, sources with small
426 P-wave angles of incidence are selected.
427
428
429
430
431
432

433 *3.1. Pre-processing*

434
435 Here, we obtain the input data and prepare it for the proper application
436 of the [Equation 1](#). Using the reference seismic catalogs (IRIS and USGS),
437 we select events that occurred during the recording period (i.e., January
438 2012 until January 2013) and which are characterized by a sufficiently high
439
440
441
442

449 magnitude to have a high signal-to-noise ratio in the records of each station.
450
451
452
453
454
455
456
457
458
459
460
461
462
463
464
465
466
467
468
469
470
471
472
473
474
475
476
477
478
479
480
481
482
483
484
485
486
487
488
489
490
491
492
493
494
495
496
497
498
499
500
501
502
503
504

160 magnitude to have a high signal-to-noise ratio in the records of each station.
161 Due to likely variations of the local seismic wavefield in space and time, we
162 evaluate the signal-to-noise ratio of each event at each of the stations.

163 For the selection of seismic events, we use the software JWEED (Java
164 version of Windows Extracted from Event Data) developed by IRIS. Based
165 on restrictions in the origin time, the location, and the magnitude, we pre-
166 select events (see [Figure 3](#)). According to their epicentral distance, we clas-
167 sify them in two groups. One group is composed of events with epicentral
168 distances between 30° and 120° , and magnitudes higher than Mw. 6; each
169 event in this group guarantees a sufficiently small P-wave ray parameter
170 (< 0.08 s/km) so that seismic energy arrives (sub)vertically at a station,
171 i.e., with incident angles $< \sim 25^\circ$ ([Kennett et al., 1995](#)). The second group
172 is composed of events with epicentral distances lower than 30° and magni-
173 tudes higher than Mw. 5. These events present a wide range of possible
174 P-wave angles of incidence. Therefore, we perform an examination analysis
175 (per station) on this second group in order to select only those events with
176 at least one P-wave phase arriving with a ray parameter smaller than the
177 adopted threshold (i.e., 0.08 s/km). The ray parameters estimated by the
178 regional velocity model ak135 ([Kennett et al., 1995](#)) are appropriate for this
179 analysis, as the seismic energy arrives to a zone with velocities lower than
180 those predicted by the model ([Casas et al., 2018](#)), deviating the ray paths
181 towards the vertical. Note that once the seismic events are selected, there is
182 no need to keep the distinction between the groups, i.e., the information pro-
183 vided by the records are equally important (no weights are assigned during
184 processing).

185 The origin time of the selected events is used to extract the seismic
186 waveforms from the records of the PV and OVDAS stations. A first estimate

505
506
507
508
509
510
511
512 of the P- and S-wave arrival times for each event is calculated using the
513 regional velocity model ak135; this estimate is then employed to manually
514
515 pick accurate P- and S-wave arrival times. These times are used to compute
516
517 the signal-to-noise ratio in the frequency domain ($FSNR = A_s/A_n$, where
518 A_s and A_n are the signal and noise amplitude spectrums, respectively) and
519
520 subsequently obtain a frequency range of a sufficiently high ratio. We request
521
522 a good ($FSNR > 4$) signal-to-noise ratio for the events to be processed, in
523
524 order to avoid high amplitudes of events we are not interested in.

525 Once we obtained the origin time of the selected events and the accurate
526
527 arrival times, and we examined the (sub)vertical incidence of the P-wave
528
529 energy and high signal-to-noise ratio of the records, we extract the vertical-
530
531 component records of the selected events at each of the used stations.

532 3.2. Processing

533 The vertical-component records of seismic events with P-wave energy
534
535 arriving (sub)vertically at a station represent an accurate estimate of the
536
537 P-wave transmission response of such propagating wavefield (provided the
538
539 discontinuities are not excessively inclined; [Nishitsuji et al. \(2016\)](#)).

540 From the frequency range of the processing previously selected for each
541
542 event at every station according to its signal-to-noise ratio in the records,
543
544 we use the frequencies higher than 0.3 Hz, a threshold defined by the in-
545
546 strumental characteristics of the PV-array stations ([Nishitsuji et al., 2014](#)).
547
548 Furthermore, we only use those frequencies which are common for all the
549
550 events, i.e., [0.3 3] Hz. In order to perform a better interpretation of the
551
552 results in depth, we segmented this frequency range in two sub-ranges, i.e.,
553
554 [0.3 0.8] Hz and [0.8 3] Hz. The separation frequency (0.8 Hz) is selected
555
556 after a trial and error approach, based on the observed coherency in the
557
558
559
560

561
562
563
564
565
566
567
568 213 results for all the stations in advanced stages of the processing.

569 214 In order to avoid the rise of high-amplitude non-physical arrivals caused
570
571 215 by cross-terms in the correlations, we extract the times between the first
572
573 216 P-wave arrival (including this first arrival) and the first S-wave arrival. As
574
575 217 an example, [Figure 4](#) shows the processing windows for the station PV04 in
576 218 the frequency range [0.8 3] Hz).

577 219 As the information provided by each of the events is equally impor-
578
579 220 tant, we normalize the processing windows according to their vertical flux
580
581 221 of seismic energy. Therefore, all the events will contribute in the summation
582 222 process in [Equation 1](#).

583 223 As suggested by [Equation 1](#), we estimate and deconvolve the ASTF
584
585 224 from each of the autocorrelated time windows. The ASTF of each event
586
587 225 is estimated by the main lobe and its secondary monotonously decreasing
588
589 226 amplitudes, as shown in [Figure 5](#) for the vertical component of station AD2
590
591 227 and the frequency range [0.3 0.8] Hz. A dominance of the main lobe in the
592
593 228 autocorrelated deconvolved traces is observed after deconvolution. These
594
595 229 features close to 0 s are amplitudes remaining from the deconvolution rele-
596
597 230 vant to the Dirac’s delta. Therefore, we remove them through windowing,
598
599 231 i.e., muting the monotonously decreasing amplitudes relevant to the 0 s
600
601 232 lobe. However, high amplitudes are still present at early times, i.e., down
602
603 233 to $\sim 10 - 15$ s. These arrivals might be multiples of reflections at the crustal
604
605 234 discontinuities and the crust-mantle boundary (the Moho). We then ap-
606
607 235 ply predictive deconvolution in order to attenuate these multiples (as also
608
609 236 implemented by [Nishitsuji et al. \(2016\)](#) for the same area).

610
611 237 SIbyA is based on the autocorrelation of time windows extracted from
612
613 238 the records of selected seismic events. Despite an appropriate selection of the
614
615 239 seismic event and the P-window, note that this autocorrelation trace could
616

617
618
619
620
621
622
623
624 contain non-physical arrivals at times equal to the time interval between
625
626 two P-wave phase arrivals (as, for example, PP or PcP phases), reducing
627
628 the quality of the results. However, these time intervals are a function of the
629
630 epicentral distance of the events. The seismic events used in this application
631
632 present a wide range of epicentral distances, so that the non-physical arrivals
633
634 are located at different times in the autocorrelations, leading to a destructive
635
636 interference of their energy during stacking (Kim et al., 2019; Tork Qashqai
637
638 et al., 2019).

639
640 In addition, converted waves (e.g., P-to-S and S-to-P) might also con-
641
642 tribute to the retrieved result in the autocorrelated traces. However, pro-
643
644 vided we correlate vertical-component data, non-physical arrivals from S-
645
646 wave converted energy are expected to be attenuated on these zero-offset
647
648 results (Delph et al., 2019). Furthermore, we choose to autocorrelate only
649
650 (sub)vertical energy on the vertical components. This further limits record-
651
652 ing S-wave arrivals; even though a transmission path from an earthquake
653
654 source to the stations might contain S-waves, the final leg of the transmis-
655
656 sion path before being detected on the vertical components of the stations
657
658 will contain little to no S-wave energy. When such arrivals are reflected
659
660 by the Earth’s free surface, and consecutively by impedance contrasts in
661
662 the subsurface, they will also be characterized by little to no conversions to
663
664 S-waves. Thus, by choosing for autocorrelation only (sub)vertical arrivals
665
666 at the stations, we naturally suppress the presence in the retrieved results
667
668 of cross-terms due to correlation of P- and S-wave arrivals thus obtaining
669
670 mainly retrieved P-waves on the vertical component and S-waves on the
671
672 horizontal components of the stations. Nevertheless, in order to provide
evidence of the attenuation of these cross terms, as well as for testing the
stability of our seismic results, we also apply SIbyA to the P and SH wave-

673
674
675
676
677
678
679
680 fields associated to each of the seismic sources (as applied by [Kim et al.](#)
681 [\(2019\)](#)). We employ the three component records at a station and the lo-
682 cation of the selected seismic sources to estimate the P and SH wavefields
683
684
685 [\(Kennett, 1991\)](#). Shallow P- and S-wave velocities are required for estimat-
686 ing these wavefields. For (sub)vertical incident seismic energy, even though
687 shallow velocities would not be accurately known, small variations of se-
688 lected velocities do not cause big changes on the results [\(Kennett, 1991\)](#).
689
690 Then, estimates of P and SH wavefields are sufficiently accurate. Thus, we
691
692 apply the same processing scheme as for the vertical component but to the
693
694 estimated wavefields. For the P wavefield, we use the same processing time
695
696 window as for the vertical-component data, i.e., enclosing the first P-wave
697
698 arrival and its seismic coda; for the SH wavefield, we use the same win-
699
700 dow size but enclosing the first S-phase arrival and its seismic coda. Note
701
702 that P- and SH-wavefield estimation requires three-component data. As we
703
704 have access to the three-component records of the PV stations only, the
705
706 results using these estimated wavefields might be significant for this array
707
708 exclusively.

709
710 The last step in the application of [Equation 1](#) is stacking the result-
711
712 ing autocorrelated traces for each station, which enhances the energy from
713
714 the stationary phase area. We use phase-weighted stacking ([Schimmel and](#)
715
716 [Paulssen, 1997](#); [Schimmel and Gallart, 2003](#)) for a better treatment of spu-
717
718 rious out-of-phase arrivals compared to the classical linear stacking ([Delph](#)
719
720 [et al., 2019](#); [Andrés et al., 2019](#)). [Figure 6a](#) and [Figure 6b](#) show the pre-stack
721
722 panel (deconvolved and windowed autocorrelated traces) and the stacked
723
724 traces for PV05 and CRI stations, which use P-wavefield data in the fre-
725
726 quency range [0.3, 0.8] Hz and vertical-component data for [0.8 3] Hz, re-
727
728 spectively. Provided the stations of each array are relatively close to each

729
730
731
732
733
734
735
736 other, we also stacked the individual retrieved reflection trace per array in
737 an attempt to further increase the signal-to-noise ratio of retrieved events..
738 [Figure 6c](#) and [Figure 6d](#) show the results for the OVDAS array using vertical-
739 component data in the [0.3 0.8] Hz frequency range and the results using
740 the P-wavefield data for the PV array in the [0.8 3] Hz frequency range,
741 respectively.
742
743
744
745

746 **4. Interpretation and discussion**

747
748
749 Aiming to compare the seismic results with the known features of the
750 subsurface, we transform the time axis of the results to depth through con-
751 struction and utilization of a velocity model. This model is composed of
752 velocities provided by the regional model ak135 for depths greater than 60
753 km, and a modified version of the model obtained by [Bohm et al. \(2002\)](#) for
754 shallower depths (see [Figure 7](#)).
755
756
757

758 [Figure 8](#) (right) shows the results for the PV and OVDAS arrays for
759 each processing frequency range and each employed source of data (i.e., ver-
760 tical component, P wavefield, and/or SH wavefield). Provided the complex
761 impedance contrast with depth expected for the area of the PPVC, and
762 the possible presence of non-physical arrivals, we only seek for the domi-
763 nant amplitudes on the obtained reflection responses (i.e., local maximum
764 amplitudes on the envelope of the resulting signal), which are potentially re-
765 lated to the main subsurface discontinuities. Average energy is computed for
766 overlapping running windows; a candidate local maximum is selected when
767 the averages of several consecutive windows are more than double the seis-
768 mic energy for earlier consecutive windows. From the maximums selected
769 automatically, we select manually the accepted local maximum amplitudes.
770
771
772
773
774
775
776
777

785
786
787
788
789
790
791
792 The lowest frequency range (i.e., [0.3 0.8] Hz) gives us the possibility
793
794 to describe the subsurface between ~ 30 and ~ 750 km depth, whereas the
795
796 results for the frequency range [0.8 3] Hz allow us to interpret the subsurface
797
798 features for depths between 10 km and the Moho. The minimum depth limit
799
800 is set by the smeared delta-function (central-lobe monotonously decreasing)
801
802 amplitudes removed after deconvolution. The maximum depth limit is set
803
804 by significant attenuation of the seismic amplitudes at later times.

805
806 The interpretation of the results for each frequency range is performed
807
808 through contrast of the seismic results and the expected location of the
809
810 known subsurface features based on the geodynamic scenario and the avail-
811
812 able geological information for the area of the PPVC (Ferrán and Martínez,
813
814 1962; Tassara et al., 2006; Farías et al., 2010; Benavente, 2010; Tapia Silva,
815
816 2010; Giambiagi et al., 2012; Bostock, 2013; Deuss and Woodhouse, 2004;
817
818 Faccenna et al., 2017; Jackson et al., 2018).

819
820 For each array, the obtained seismic results (see Figure 8, right) for
821
822 the vertical component and the P and/or SH wavefields show dominant
823
824 amplitudes (i.e., local maximum amplitudes on the waveform envelopes) in
825
826 common, which we classify as potential subsurface impedance contrasts.

827
828 Note that the SH-wavefield results are not shown in Figure 8a (i.e., for
829
830 [0.3 0.8] Hz frequency range). The SH-wavefield results are not coherent over
831
832 the stations of the PV array. This might be caused by higher attenuation of
833
834 the S-wave energy in comparison to the P-wave energy in this volcanic zone
835
836 for the vertically incident seismic energy; then, attenuation would seriously
837
838 affect S-wave coherency on the autocorrelations traces. Therefore, for the
839
840 lower frequency range, the interpretation of the potential subsurface features
841
842 is performed using the vertical-component and P-wavefield results for the
843
844 PV array and the vertical-component results for the OVDAS array.

841
842
843
844
845
846
847
848 For the shallowest depths in the results, the multiples, although attenu-
849 ated after predictive deconvolution, might still be significant, likely challeng-
850 ing the identification of the amplitudes representing primaries. Thus, for the
851 shallowest depths, our interpretation is based on analyses of the spatial cor-
852 relation between the arrivals in the seismic results and the known subsurface
853 discontinuities. For arrivals at the later times, two considerations limit the
854 possibility of them being multiples. First, the target volcanic area presents
855 high attenuation effects (Manassero et al., 2014); therefore, long paths are
856 highly attenuated. Second, based on Zoeppritz's equations (Shuey, 1985)
857 and provided vertical incidence of the propagating seismic energy, refracted
858 (i.e., transmitted) energy represent $\sim 90\%$ of such propagated energy. Thus,
859 the seismic energy relevant to later multiples or higher-order multiples is sig-
860 nificantly reduced. These effects led us to infer that multiples at later times
861 are highly attenuated, making those multiples most likely unidentifiable.

862 For the lower frequency range, the interpretation of the shallowest (down
863 to ~ 200 km) section of the subsurface is the most intricate as a consequence
864 of the number of discontinuities reflecting energy and the likely presence of
865 multiples. However, the close location of the identified features in the seismic
866 results and the known subsurface features lead us to the interpretation of
867 the Moho discontinuity at ~ 50 km depth, a low-velocity zone (LVZ) at ~ 100
868 km depth down to the top of the subducting slab at ~ 120 km depth, and
869 the bottom of the subducting slab at ~ 200 km. Even though the available
870 information points to the lithosphere-asthenosphere boundary being at ~ 75
871 km depth (Tassara et al., 2006; Giambiagi et al., 2012), it emerges ambiguous
872 in our results (see the shallowest empty rectangle in Figure 8a) likely due to
873 hydration originating by the subducting slab at these depths (Gilbert et al.,
874 2006), or the presence of multiples from the crustal structure.

897
898
899
900
901
902
903
904 The results for this frequency range evidence the presence of the Lehmann
905 discontinuity (Deuss and Woodhouse, 2004) at ~ 270 km depth, the 410 km
906 and 660 km discontinuities, as well as three extra discontinuities named
907 Reflector A, Reflector B, and Reflector C in Figure 8a. Reflector A is lo-
908 cated around 325 km depth; we think this is relevant to the discontinuity
909 previously identified by Havens (1999) for the same area, which might be
910 an evidence of ancient subducted oceanic crust (Williams and Revenaugh,
911 2005). Reflector B is located at ~ 480 km depth; given its location and rel-
912 atively low amplitude, it is probably a multiple from a shallower reflector.
913 Reflector C is located at ~ 600 km depth; its distinguished amplitude guides
914 us to think it is not a multiple of any previous arrival. The bottom of the
915 transition zone (i.e., around 660 km depth) would present its own topog-
916 raphy as a consequence of an ancient subducting slab moving horizontally
917 at these depths, then undergoing thickening and folding (Faccenna et al.,
918 2017). Reflector C might be indicating the top of this feature.

927 The OVDAS array is located ~ 6 km to the north of the PV array, com-
928 posed of half the stations of the PV array. The results for OVDAS array
929 for the two used frequency ranges are similar to those for the PV array,
930 which evidences that main subsurface features do not change largely along
931 the volume separating them.

935 Even though dipping structures in the subsurface restrict the reflection
936 energy arriving at the surface, we clearly identify the depth of the top and
937 bottom of the subducting slab. Therefore, two hypotheses arise. One hy-
938 pothesis suggests a stair-like subduction (Figure 2b-3), according to which
939 the top and the bottom of the oceanic slab present horizontal (or gently
940 inclined) regions. This hypothesis, though, would not explain the lack of
941 seismicity at the longitude of the stations and depths of analysis (*US Geo-*
942
943
944
945
946

953
954
955
956
957
958
959
960 *logical Survey*; Nishitsuji et al. (2016)). A second hypothesis proposes a slab
961 deformation in the form of detachment, shearing, necking, or any combina-
962 tion (see Figure 2b-4, Nishitsuji et al. (2016)). However, more information
963 is required to elucidate the proper interpretation.
964

965
966 For the second range of frequencies (i.e., [0.8 3] Hz), we also use vertical-
967 component data for the PV and OVDAS arrays, as well as P- and SH-
968 wavefield data for PV array. In this case, coherent similar results are ob-
969 tained from all those sources of data (see Figure 8b, right). Note that,
970 opposite to [0.3 0.8] Hz results, SH results for [0.8 3] Hz also provide in-
971 terpretable information about the subsurface reflectors. Even though the
972 higher the frequencies, the greater the expected attenuation effect (Schön,
973 2015), the interpreted propagation distances are shorter for this frequency
974 range; therefore, coherent energy arises on the SH results.
975
976

977
978 The interpretation of the results for the second frequency range is based
979 on the average depth of the identified reflectors, the available scientific infor-
980 mation about the subsurface in the PPVC (e.g., Ferrán and Martínez (1962);
981 Benavente (2010); González-Vidal et al. (2018)), the proposed structure of
982 the crust for the area (Gilbert et al., 2006; Tassara et al., 2006; Farías et al.,
983 2010; Giambiagi et al., 2012), and the physics of magma storage in the crust
984 (Jackson et al., 2018).
985
986

987
988 The results for both arrays for this frequency range indicate six domi-
989 nant amplitudes. Those located at ~ 13 , ~ 18 , and ~ 37 km depth agree with
990 the depth of intra-discontinuity in the upper crust (rigid-ductile disconti-
991 nuity), the intra-crustal discontinuity (between the upper and lower crust),
992 and the intra-discontinuity in the lower crust (rigid-ductile discontinuity),
993 respectively.
994
995

996
997 Jackson et al. (2018) models the formation, storage, and chemical differ-
998
999
1000

1009
1010
1011
1012
1013
1014
1015
1016 427 entiation of magma in the Earth’s crust. According to the physics of magma
1017 428 storage, the melt fraction is not homogeneously distributed with depth. A
1018 429 high percentage of melt is located in the very upper part of a reservoir, a
1019 430 low percentage is located through most of the reservoir, while a solid area is
1020 431 present in the lowest part. The seismic results are most probably evidence
1021 432 of the solid lower section of the reservoir (Jackson et al., 2018). Because
1022 433 of this, we speculate that magma could be stored right above some of the
1023 434 identified reflectors (see Figure 8b), in particular the one located at ~ 28 km
1024 435 depth, as it is not associated with any of the main discontinuities of the
1025 436 crust.

1031
1032 437 The seismic results also show the location of two reflectors at ~ 46 and
1033 438 ~ 52 km depth; we interpret these reflectors as the top of the MASH (Melt-
1034 439 ing, Assimilation, Storage and Homogenization zone, previously imaged by
1035 440 Gilbert et al. (2006) for this area) and the Moho, respectively. The MASH
1036 441 zone is composed of low-velocity zones (Hildreth and Moorbath, 1988) which
1037 442 supports the negative amplitudes of the reflector identified at ~ 46 km depth,
1038 443 as well as the presence of a blurred Moho arrival (Gilbert et al., 2006). Fi-
1039 444 nally, following Cashman et al. (2017) and González-Vidal et al. (2018), we
1040 445 interpret those areas between zones of likely storage of magma as transfer
1041 446 zones via dikes.

1047 447 Our results support the information obtained for the subsurface in the
1048 448 area (Yuan et al., 2006; Ward et al., 2013; González-Vidal et al., 2018)
1049 449 which indicates (although with a limited resolution) low-velocity zones for
1050 450 approximately the same range of depths.

1051 451 The resolution of the results is a function of the uncertainties in the ve-
1052 452 locity model, as well as the quality of the data and the processing applied.
1053 453 We estimate the uncertainty of our interpretation based on the width of the

1065
1066
1067
1068
1069
1070
1071
1072 identified features in the seismic results. This strategy not only accounts
1073
1074 for the vertical resolution, according to which the pulse relevant to a dis-
1075
1076 continuity might be wider in case of small differences in the arrival times at
1077
1078 the traces to be stacked, but also for the horizontal resolution. The energy
1079
1080 from the Fresnel zone interferes constructively to provide the resulting seis-
1081
1082 mic trace. This zone is larger for deeper discontinuities. This means that a
1083
1084 zone that we describe as vertically below a station should be understood as
1085
1086 starting vertically below a station and extending laterally on both sides of
1087
1088 the vertical to include the Fresnel zone. As a result, a zone that we interpret
1089
1090 as (sub-)horizontal or locally deformed below a station, might actually be
1091
1092 lying away from the vertical up to the extend of half the Fresnel zone at that
1093
1094 depth. The features on the results for the lower frequency range present an
1095
1096 average width of ~ 12 km for depths below 350 km, and ~ 33 km for higher
1097
1098 depths; the features for the higher frequency range present an average width
1099
1100 of ~ 2.7 km. Provided the close spatial correlation of our results with the
1101
1102 geological information available for the area, we infer that the (composed
1103
1104 -vertical and horizontal) resolution of our results is sufficiently high.

1105
1106 Because the interpretations performed in this article are based on the
1107
1108 available scientific information for the area of the PPVC in addition to
1109
1110 the obtained seismic results, [Figure 8](#) represents a reasonable subsurface
1111
1112 model for depths between 10 and 750 km. We expect this model to be
1113
1114 used as a starting point for more accurate estimation of the locations of the
1115
1116 subsurface features. It is also worth noting the importance of developing a
1117
1118 high-resolution (P- and S-wave) velocity model for the area of the PPVC,
1119
1120 which would allow an appropriate location of seismic events in depth as well
as an efficient removal of multiples, enhancing the quality of the results.
Therefore, more research (particularly, local seismic velocity -or attenuation-

1121
1122
1123
1124
1125
1126
1127
1128 tomography studies) is required to accurately locate and characterize the
1129
1130 regions of magma storage.

1131 1132 483 **5. Conclusions**

1133
1134
1135 484 Even though the Planchón-Peteroa Volcanic Complex (PPVC) is one
1136 485 of the most hazardous volcanic systems in the Central Andes, its internal
1137
1138 486 processes, structures, dynamics, and their relation are still not satisfactorily
1139
1140 487 understood.

1141 488 We applied seismic interferometry by autocorrelation to regional and
1142
1143 489 teleseismic earthquake arrivals recorded by nine stations deployed in the
1144
1145 490 area of the PPVC (six in Argentina and three in Chile) during 2012. The
1146
1147 491 events are selected according to their location, magnitude, angle of incidence
1148
1149 492 of the P-wave energy, the signal-to-noise ratio on the results, and the related
1150
1151 493 useful frequency range. The interferometric results represent virtual reflec-
1152
1153 494 tion measurements from virtual sources co-located with each of the array
1154
1155 495 stations, where the virtual sources emit energy (sub) vertically down. With
1156
1157 496 the virtual reflection measurement, we aimed to shed extra light on the sub-
1158
1159 497 surface below the PPVC. In order to perform an appropriate description of
1160
1161 498 the subsurface structures below the stations, we used two frequency ranges
1162
1163 499 ([0.3 0.8] Hz and [0.8 3] Hz) which are sensitive to different range of depths.

1164
1165 500 We used the lower frequency range ([0.3 0.8] Hz) to infer tectonic fea-
1166
1167 501 tures, i.e., the Moho (at ~ 50 km depth), the lithosphere-asthenosphere
1168
1169 502 boundary (~ 75 km), the top of a low-velocity zone at ~ 100 km depth, the
1170
1171 503 top and bottom of the subducting slab (~ 120 and ~ 200 km), the Lehmann
1172
1173 504 discontinuity at ~ 270 km, a discontinuity at ~ 330 km depth, the 410 km dis-
1174
1175 505 continuity, and a layer between ~ 600 and ~ 660 km depth likely originating
1176

1177
1178
1179
1180
1181
1182
1183
1184 from accumulated ancient subducting slab at these depths.

1185 Based on the results for the higher frequencies (i.e., [0.8 3] Hz) and
1186
1187 previous geological, geochemical, and geophysical information, we proposed
1188
1189 a model which describes the structure of the crust and the subsurface regions
1190 storing magma bodies down to the Moho. We suggested three regions of
1191 magma emplacement right above ~ 13 km, ~ 28 km, and ~ 37 km depth,
1192 respectively.
1193

1194
1195 The present work provides valuable information about the subsurface
1196
1197 conditions of an active volcanic system -the CVPP. We expect the obtained
1198
1199 knowledge to be employed in future research aiming to better understand
1200 the dynamics of the CVPP.
1201

1202 **6. Acknowledgments**

1203
1204
1205 The authors thank SERNAGEOMIN for providing earthquake data recorded
1206
1207 by the OVDAS seismic network. The authors thank IRIS-PASSCAL for
1208
1209 providing the seismic equipment deployed in Argentina, and the Argentine
1210
1211 Ministry of Science, Technology and Production Innovation for the finan-
1212
1213 cial support connected to the transportation of the equipment. The authors
1214
1215 thank Pierre Auger Observatory and the Department of Civil Defense of
1216
1217 Malarge for the help during the data acquisition. The authors thank two
1218
1219 anonymous reviewers for their valuable comments that helped improve the
1220
1221 manuscript.
1222

1223 **References**

1224 Andrés, J., Draganov, D., Schimmel, M., Ayarza, P., Palomeras, I., Ruiz,
1225
1226 M., Carbonell, R., 2019. Lithospheric image of the Central Iberian Zone
1227
1228
1229
1230
1231
1232

- 1233
1234
1235
1236
1237
1238
1239
1240 (Iberian Massif) using Global-Phase Seismic Interferometry. *Solid Earth*
1241
1242 Discussions doi:[10.5194/se-2019-107](https://doi.org/10.5194/se-2019-107).
1243
1244 Benavente, O., 2010. Actividad Hidrotermal asociada a los Complejos
1245 Volcánicos Planchón-Peteroa y Descabezado Grande-Quizapu-Cerro Azul,
1246 36S y 37°S, Zona Volcánica Sur, Chile. Universidad de Chile URL:
1247 <http://repositorio.uchile.cl/handle/2250/103949>.
1248
1249
1250 Benavente, O., Tassi, F., Reich, M., Aguilera, F., Capecchiacci, F.,
1251
1252 Gutiérrez, F., Vaselli, O., Rizzo, A., 2016. Chemical and isotopic fea-
1253
1254 tures of cold and thermal fluids discharged in the Southern Volcanic Zone
1255
1256 between 32.5S and 36S: Insights into the physical and chemical processes
1257
1258 controlling fluid geochemistry in geothermal systems of Central Chile.
1259
1260 Chemical Geology doi:[10.1016/j.chemgeo.2015.11.010](https://doi.org/10.1016/j.chemgeo.2015.11.010).
1261
1262 Bohm, M., Lüth, S., Echtler, H., Asch, G., Bataille, K., Bruhn, C., Ri-
1263
1264 etbrock, A., Wigger, P., 2002. The Southern Andes between 36 and
1265
1266 40S latitude: Seismicity and average seismic velocities. *Tectonophysics*
1267
1268 doi:[10.1016/S0040-1951\(02\)00399-2](https://doi.org/10.1016/S0040-1951(02)00399-2).
1269
1270
1271 Bostock, M.G., 2013. The Moho in subduction zones. doi:[10.1016/j.](https://doi.org/10.1016/j.tecto.2012.07.007)
1272
1273 [tecto.2012.07.007](https://doi.org/10.1016/j.tecto.2012.07.007).
1274
1275
1276 Boullenger, B., Verdel, A., Paap, B., Thorbecke, J., Draganov, D., 2014.
1277
1278 Studying CO₂ storage with ambient-noise seismic interferometry: A
1279
1280 combined numerical feasibility study and field-data example for Ket-
1281
1282 zin, Germany. *Geophysics* 80, Q1–Q13. doi:[https://doi.org/10.1190/](https://doi.org/10.1190/geo2014-0181.1)
1283
1284 [geo2014-0181.1](https://doi.org/10.1190/geo2014-0181.1).
1285
1286
1287 Casas, J., Draganov, D., Badi, G., Manassero, M., Olivera Craig, V., Franco
1288

1289
1290
1291
1292
1293
1294
1295
1296 554 Marín, L., Gómez, M., Ruigrok, E., 2019. Seismic interferometry ap-
1297 555 plied to local fracture seismicity recorded at Planchón-Peteroa Volcanic
1298 556 Complex, Argentina-Chile. *Journal of South American Earth Sciences*
1300 557 doi:[10.1016/j.jsames.2019.03.012](https://doi.org/10.1016/j.jsames.2019.03.012).

1302
1303 558 Casas, J.A., Badi, G., Manassero, M., Gomez, P., Draganov, D., Ruzzante,
1304 559 J., 2014. Characterization of Seismo-volcanic Activity in Peteroa Vol-
1305 560 cano, Central Andes Argentina-Chile. *Earth Sciences Research Journal*
1306 561 18, 335–336. URL: [https://www.researchgate.net/publication/](https://www.researchgate.net/publication/299381773)
1307 562 [299381773](https://www.researchgate.net/publication/299381773){_}Characterization{_
1308 563 }of{_
1309 564 }Seismo-volcanic{_
1310 565 }Activity{_
1311 566 }in{_
1312 567 }Peteroa{_
1313 568 }Vol

1314 563 Casas, J.A., Mikesell, T.D., Draganov, D., Lepore, S., Badi, G.A., Franco,
1315 564 L., Gómez, M., 2018. Shallow S-Wave Velocity Structure from Am-
1316 565 bient Seismic Noise at Planchón-Peteroa Volcanic Complex, Argentina-
1317 566 Chile. *Bulletin of the Seismological Society of America* 108, 2183–2198.
1318 567 doi:<https://doi.org/10.1785/0120170281>.

1319
1320 568 Cashman, K.V., Sparks, R.S.J., Blundy, J.D., 2017. Vertically extensive and
1321 569 unstable magmatic systems: A unified view of igneous processes. *Science*
1322 570 doi:[10.1126/science.aag3055](https://doi.org/10.1126/science.aag3055).

1323
1324
1325 571 Claerbout, J.F., 1968. Synthesis of a layered medium from its acoustic trans-
1326 572 mission response. *GEOPHYSICS* doi:[10.1016/0022-0248\(91\)90961-4](https://doi.org/10.1016/0022-0248(91)90961-4).

1327
1328
1329 573 Delph, J.R., Levander, A., Niu, F., 2019. Constraining crustal properties
1330 574 using receiver functions and the autocorrelation of earthquakegenerated
1331 575 body waves. *Journal of Geophysical Research: Solid Earth* doi:[10.1029/](https://doi.org/10.1029/2019JB017929)
1332 576 [2019JB017929](https://doi.org/10.1029/2019JB017929).

1333
1334
1335
1336 577 Deuss, A., Woodhouse, J.H., 2004. The nature of the Lehmann discontinuity
1337
1338

- 1345
1346
1347
1348
1349
1350
1351
1352 578 from its seismological Clapeyron slopes. *Earth and Planetary Science*
1353 579 Letters doi:[10.1016/j.epsl.2004.06.021](https://doi.org/10.1016/j.epsl.2004.06.021).
- 1355
1356 580 Draganov, D.S., Wapenaar, K., Mulder, W., Singer, J., Verdel, A., 2007. Re-
1357 581 trieval of reflections from seismic background-noise measurements. *Geo-*
1358 582 *physical Research Letters* 34. doi:[10.1029/2006GL028735](https://doi.org/10.1029/2006GL028735).
- 1361
1362 583 Elissondo, M., Farías, C., 2016. Volcanic Risk assessment in Ar-
1363 584 gentina, in: *Cities on Volcanoes IX*, Puerto Varas, Chile. URL:
1364 585 [https://www.citiesonvolcanoes9.com/fileadmin/user_{_}upload/
1365 586 S1.4_{_}Elissondo.pdf](https://www.citiesonvolcanoes9.com/fileadmin/user/_upload/S1.4_}Elissondo.pdf).
- 1368
1369 587 Faccenna, C., Oncken, O., Holt, A.F., Becker, T.W., 2017. Initiation of
1370 588 the Andean orogeny by lower mantle subduction. *Earth and Planetary*
1371 589 *Science Letters* doi:[10.1016/j.epsl.2017.01.041](https://doi.org/10.1016/j.epsl.2017.01.041).
- 1373
1374 590 Fan, Y., Snieder, R., 2009. Required source distribution for interferometry
1375 591 of waves and diffusive fields. *Geophysical Journal International* 179, 1232–
1376 592 1244. doi:[10.1111/j.1365-246X.2009.04358.x](https://doi.org/10.1111/j.1365-246X.2009.04358.x).
- 1378
1379 593 Farías, M., Comte, D., Charrier, R., Martinod, J., David, C., Tassara, A.,
1380 594 Tapia, F., Fock, A., 2010. Crustalscale structural architecture in central
1381 595 Chile based on seismicity and surface geology: Implications for Andean
1382 596 mountain building. *Tectonics* 29. doi:[10.1029/2009TC002480](https://doi.org/10.1029/2009TC002480).
- 1385
1386 597 Ferrán, O.L.G., Martínez, M.V., 1962. Reconocimiento geológico de la
1387 598 Cordillera de los Andes entre los paralelos 35 y 38 sur, in: *Anales de*
1388 599 *la Facultad de Ciencias Físicas y Matemáticas*, p. 19.
- 1391
1392 600 Giambiagi, L., Mescua, J., Bechis, F., Tassara, A., Hoke, G., 2012. Thrust
1393 601 belts of the southern Central Andes: Along-strike variations in shortening,

1401
1402
1403
1404
1405
1406
1407
1408 602 topography, crustal geometry, and denudation. Bulletin of the Geological
1409 603 Society of America doi:[10.1130/B30609.1](https://doi.org/10.1130/B30609.1).

1411
1412 604 Gilbert, H., Beck, S., Zandt, G., 2006. Lithospheric and upper mantle struc-
1413 605 ture of central Chile and Argentina. Geophysical Journal International
1414 606 doi:[10.1111/j.1365-246X.2006.02867.x](https://doi.org/10.1111/j.1365-246X.2006.02867.x).

1417 607 González-Vidal, D., Obermann, A., Tassara, A., Bataille, K., Lupi, M.,
1418 608 2018. Crustal model of the Southern Central Andes derived from ambient
1420 609 seismic noise Rayleigh-wave tomography. Tectonophysics doi:[10.1016/j.](https://doi.org/10.1016/j.tecto.2018.07.004)
1421 610 [tecto.2018.07.004](https://doi.org/10.1016/j.tecto.2018.07.004).

1424 611 Gorbatov, A., Saygin, E., Kennett, B.L., 2013. Crustal properties from
1425 612 seismic station autocorrelograms. Geophysical Journal International
1427 613 doi:[10.1093/gji/ggs064](https://doi.org/10.1093/gji/ggs064).

1429 614 Guzmán, C., Hucailuk, C., Tamasi, M., Martínez Bogado, M., Torres,
1431 615 D., 2013. Anomalías Encontradas en los Parámetros Registrados en la
1432 616 Estación de Medición de la Terma del Volcán Peteroa, in: Actas de ICES
1434 617 IX, pp. 186–194. URL: <http://www.uncuyo.edu.ar/ices/e-ices-2>.

1436 618 Haller, M.J., Coscarella, M., 2011. Análisis probabilístico
1438 619 del riesgo de erupción del volcán Peteroa mediante la apli-
1439 620 cación de mezcla de distribuciones exponenciales. Nat. Haz-
1441 621 ards Earth Syst. Sci 9, 425–431. URL: [https://www.](https://www.researchgate.net/profile/Miguel_Haller/publication/248702232_Analisis_probabilistico_del_riesgo_de_erupcion_del_volcan_links/0046352ea9820434d700000/Analisis-probabilist)
1442 622 [researchgate.net/profile/Miguel_Haller/publication/](https://www.researchgate.net/profile/Miguel_Haller/publication/248702232_Analisis_probabilistico_del_riesgo_de_erupcion_del_volcan_links/0046352ea9820434d700000/Analisis-probabilist)
1444 623 [248702232_Analisis_probabilistico_del_riesgo_de_erupcion_del_volcan](https://www.researchgate.net/profile/Miguel_Haller/publication/248702232_Analisis_probabilistico_del_riesgo_de_erupcion_del_volcan_links/0046352ea9820434d700000/Analisis-probabilist)
1446 624 [links/0046352ea9820434d700000/Analisis-probabilist](https://www.researchgate.net/profile/Miguel_Haller/publication/248702232_Analisis_probabilistico_del_riesgo_de_erupcion_del_volcan_links/0046352ea9820434d700000/Analisis-probabilist).

1448 625 Haller, M.J., Ostera, H.A., Pesce, A.H., Gardini, M., Folguera, A., 1994.

- 1457
1458
1459
1460
1461
1462
1463
1464 626 Vulcanoestratigrafía reciente y eruptividad del volcán Peteroa, in: Con-
1465 627 greso Geológico Chileno, pp. 319–323.
- 1467 628 Haller, M.J., Risso, C., 2011. La erupción del volcán peteroa (3515's, 7018'o)
1469 629 del 4 de septiembre de 2010. Revista de la Asociacion Geologica Ar-
1470 630 gentina URL: [http://ppct.caicyt.gov.ar/index.php/raga/article/](http://ppct.caicyt.gov.ar/index.php/raga/article/view/489)
1472 631 [view/489](http://ppct.caicyt.gov.ar/index.php/raga/article/view/489).
- 1474 632 Havens, E., 1999. Mantle discontinuities beneath South and Central Amer-
1476 633 ica. Ph.D. thesis. University of California.
- 1478 634 Hildreth, W., Moorbath, S., 1988. Crustal contributions to arc magmatism
1480 635 in the Andes of Central Chile. Contributions to Mineralogy and Petrology
1482 636 doi:[10.1007/BF00372365](https://doi.org/10.1007/BF00372365).
- 1484 637 Jackson, M.D., Blundy, J., Sparks, R.S., 2018. Chemical differentiation,
1485 638 cold storage and remobilization of magma in the Earth's crust. doi:[10.](https://doi.org/10.1038/s41586-018-0746-2)
1487 639 [1038/s41586-018-0746-2](https://doi.org/10.1038/s41586-018-0746-2).
- 1489 640 Kennett, B.L., 1991. The Removal of Free Surface Interactions From Three-
1491 641 Component Seismograms. Geophysical Journal International doi:[10.](https://doi.org/10.1111/j.1365-246X.1991.tb02501.x)
1492 642 [1111/j.1365-246X.1991.tb02501.x](https://doi.org/10.1111/j.1365-246X.1991.tb02501.x).
- 1494 643 Kennett, B.L.N., Engdahl, E.R., Buland, R., 1995. Constraints on seismic
1496 644 velocities in the Earth from traveltimes. Geophysical Journal International
1497 645 doi:[10.1111/j.1365-246X.1995.tb03540.x](https://doi.org/10.1111/j.1365-246X.1995.tb03540.x).
- 1500 646 Kim, D., Brown, L.D., Árnason, K., Águstsson, K., Blanck, H., 2017.
1501 647 Magma reflection imaging in Krafla, Iceland, using microearthquake
1502 648 sources. Journal of Geophysical Research: Solid Earth doi:[10.1002/](https://doi.org/10.1002/2016JB013809)
1504 649 [2016JB013809](https://doi.org/10.1002/2016JB013809).

- 1513
1514
1515
1516
1517
1518
1519
1520 650 Kim, D., Keranen, K.M., Abers, G.A., Brown, L.D., 2019. Enhanced Res-
1521 651 olution of the Subducting Plate Interface in Central Alaska From Auto-
1522 652 correlation of Local Earthquake Coda. *Journal of Geophysical Research:*
1523 653 *Solid Earth* doi:[10.1029/2018JB016167](https://doi.org/10.1029/2018JB016167).
- 1526
1527 654 Manassero, M., Badi, G., Casas, J.A., Gomez, M., Draganov, D.,
1528 655 Ruzzante, J., 2014. Seismic attenuation around Peteroa Vol-
1529 656 cano, Argentina. *Earth Sciences Research Journal* 18, 341–
1530 657 342. URL: [https://www.researchgate.net/publication/
1531 658 299388368-{}Seismic-{}attenuation-{}around-{}Peteroa-{}Volcano-{}Argentina](https://www.researchgate.net/publication/299388368-{}Seismic-{}attenuation-{}around-{}Peteroa-{}Volcano-{}Argentina).
- 1535 659 Naranjo, J.A., Haller, M.J., Ostera, H.A., Pesce, A.H., Sruoga, P., 1999.
1536 660 Geologia y peligros del Complejo Volcánico Planchón-Peteroa, Andes del
1537 661 Sur (3515'S), Región del Maule, Chile-Provincia de Mendoza, Argentina.
1538 662 Servicio Nacional de Geología y Minería.
- 1541
1542 663 Nishitsuji, Y., Ruigrok, E., Gomez, M., Draganov, D., 2014.
1543 664 Global-phase H/V spectral ratio for delineating the basin in
1544 665 the Malargue Region, Argentina. *Seismological Research Let-*
1545 666 *ters* 85, 1004–1011. URL: [http://resolver.tudelft.nl/uuid:
1546 667 e71c7bf6-6ade-46ed-b073-324d3dd7f99b](http://resolver.tudelft.nl/uuid:e71c7bf6-6ade-46ed-b073-324d3dd7f99b).
- 1550 668 Nishitsuji, Y., Ruigrok, E., Gomez, M., Wapenaar, K., Draganov,
1551 669 D., 2016. Reflection imaging of aseismic zones of the Nazca
1552 670 slab by global-phase seismic interferometry. *Interpretation* 4, SJ1–
1553 671 SJ16. URL: <http://library.seg.org/doi/10.1190/INT-2015-0225.1>,
1554 672 doi:[10.1190/INT-2015-0225.1](https://doi.org/10.1190/INT-2015-0225.1).
- 1558
1559 673 Olivera Craig, V., 2017. Relocation of fracture seismicity in Planchón-
1560 674 Peteroa Volcanic Complex through optimization of the arrival-times iden-

- 1569
1570
1571
1572
1573
1574
1575
1576 675 tification and joint location techniques. Graduate thesis. Universidad Na-
1577 676 cional de La Plata .
- 1579
1580 677 Oren, C., Nowack, R.L., 2017. Seismic body-wave interferometry using noise
1581 678 autocorrelations for crustal structure. *Geophysical Journal International*
1582 679 doi:[10.1093/gji/ggw394](https://doi.org/10.1093/gji/ggw394).
- 1585
1586 680 Ramires, A., Elissonde, A., Trombotto Liaudat, D., 2013. Posibles escenarios
1587 681 de riesgo frente a la caída de cenizas volcánicas, en el modelo ganadero de
1588 682 la cuenca alta y media del Rio Grande, Malargüe, Mendoza, in: *Actas de*
1589 683 *IX*, pp. 304–320. URL: <http://www.uncuyo.edu.ar/ices/e-ices-2>.
- 1592
1593 684 Ruigrok, E., Draganov, D., Gomez, M., Ruzzante, J., Torres, D., Pumarega,
1594 685 I.L., Barbero, N., Ramires, A., Ganan, A.R.C., van Wijk, K., 2012.
1595 686 Malargüe seismic array: Design and deployment of the temporary ar-
1596 687 ray. *The European Physical Journal Plus* 127, 126. doi:[https://doi.](https://doi.org/10.1140/epjp/i2012-12126-7)
1598 688 [org/10.1140/epjp/i2012-12126-7](https://doi.org/10.1140/epjp/i2012-12126-7).
- 1600
1601 689 Ruigrok, E., Wapenaar, K., 2012. Global-phase seismic interferometry un-
1602 690 veils P-wave reflectivity below the Himalayas and Tibet. *Geophysical*
1603 691 *Research Letters* 39. doi:[10.1029/2012GL051672](https://doi.org/10.1029/2012GL051672).
- 1606
1607 692 Schimmel, M., Gallart, J., 2003. The use of instantaneous polarization at-
1608 693 tributes for seismic signal detection and image enhancement. *Geophysical*
1609 694 *Journal International* doi:[10.1046/j.1365-246X.2003.02077.x](https://doi.org/10.1046/j.1365-246X.2003.02077.x).
- 1611
1612 695 Schimmel, M., Paulssen, H., 1997. Noise reduction and detection of weak,
1613 696 coherent signals through phase-weighted stacks. *Geophysical Journal In-*
1614 697 *ternational* doi:[10.1111/j.1365-246X.1997.tb05664.x](https://doi.org/10.1111/j.1365-246X.1997.tb05664.x).

- 1625
1626
1627
1628
1629
1630
1631
1632 698 Schön, J.H., 2015. Physical properties of rocks: Fundamentals and principles
1633 of petrophysics. volume 65. Elsevier.
1634 699
- 1635
1636 700 Shuey, R.T., 1985. Simplification of the Zoeppritz equations. Geophysics
1637 doi:[10.1190/1.1441936](https://doi.org/10.1190/1.1441936).
1638 701
- 1639
1640 702 Stern, C.R., 2004. Active Andean volcanism: its geologic and tectonic set-
1641 ting. Revista geológica de Chile doi:[10.4067/S0716-02082004000200001](https://doi.org/10.4067/S0716-02082004000200001).
1642 703
- 1643
1644 704 Tapia Silva, F.F., 2010. Análisis estructural del sector occidental de la faja
1645 plegada y corrida de Malargüe en el curso superior del río Colorado de
1646 Lontué (35°18'y 35°23's), Región del Maule, Chile. Universidad de Chile
1647 URL: <http://repositorio.uchile.cl/handle/2250/103738>.
1648 707
- 1649
1650 708 Tassara, A., Götze, H.J., Schmidt, S., Hackney, R., 2006. Three-dimensional
1651 density model of the Nazca plate and the Andean continental margin.
1652 Journal of Geophysical Research: Solid Earth doi:[10.1021/ic201714c](https://doi.org/10.1021/ic201714c).
1653 710
- 1654
1655 711 Tassi, F., Aguilera, F., Benavente, O., Paonita, A., Chiodini, G., Caliro,
1656 S., Agosto, M., Gutierrez, F., Capaccioni, B., Vaselli, O., Caselli, A.,
1657 712 Saltori, O., 2016. Geochemistry of fluid discharges from Peteroa volcano
1658 (Argentina-Chile) in 2010-2015: Insights into compositional changes re-
1659 713 lated to the fluid source region(s). Chemical Geology doi:[10.1016/j.](https://doi.org/10.1016/j.chemgeo.2016.04.007)
1660 714 [chemgeo.2016.04.007](https://doi.org/10.1016/j.chemgeo.2016.04.007).
1661 715
1662 716
- 1663
1664
1665
1666 717 Tork Qashqai, M., Saygin, E., Kennett, B.L., 2019. Crustal Imaging With
1667 Bayesian Inversion of Teleseismic P Wave Coda Autocorrelation. Journal
1668 718 of Geophysical Research: Solid Earth doi:[10.1029/2018JB017055](https://doi.org/10.1029/2018JB017055).
1669 719
- 1670
1671 720 Tormey, D., 1989. Geologic history of the active Azufre-Planchon-Peteroa
1672
1673
1674
1675
1676
1677
1678
1679
1680

- 1681
1682
1683
1684
1685
1686
1687
1688 721 volcanic center (3515'S, Southern Andes) with implications for the devel-
1689 722 opment of compositional gaps. *Asoc. Gel. Arg. Rev* , 420–430.
- 1691
1692 723 Wapenaar, K., 2003. Synthesis of an inhomogeneous medium from its acous-
1693 724 tic transmission response. *GEOPHYSICS* doi:[10.1190/1.1620649](https://doi.org/10.1190/1.1620649).
- 1695
1696 725 Wapenaar, K., 2004. Retrieving the elastodynamic Green's function of an
1697 726 arbitrary inhomogeneous medium by cross correlation. *Physical Review*
1698 727 *Letters* 93. doi:[10.1103/PhysRevLett.93.254301](https://doi.org/10.1103/PhysRevLett.93.254301).
- 1700
1701 728 Wapenaar, K., Fokkema, J., 2006. Green's function representations for seis-
1702 729 mic interferometry. *GEOPHYSICS* doi:[10.1190/1.2213955](https://doi.org/10.1190/1.2213955).
- 1704
1705 730 Ward, K.M., Porter, R.C., Zandt, G., Beck, S.L., Wagner, L.S., Minaya, E.,
1706 731 Tavera, H., 2013. Ambient noise tomography across the Central Andes.
1707 732 *Geophysical Journal International* doi:[10.1093/gji/ggt166](https://doi.org/10.1093/gji/ggt166).
- 1709
1710 733 Williams, Q., Revenaugh, J., 2005. Ancient subduction, mantle eclogite,
1711 734 and the 300 km seismic discontinuity. *Geology* doi:[10.1130/G20968.1](https://doi.org/10.1130/G20968.1).
- 1713
1714 735 Yuan, X., Asch, G., Bataille, K., Bock, G., Bohm, M., Echtler, H., Kind,
1715 736 R., Oncken, O., Wölbern, I., 2006. Deep seismic images of the Southern
1717 737 Andes. *Geological Society of America Special Papers* doi:[10.1130/2006.](https://doi.org/10.1130/2006.2407(03))
1718 738 [2407\(03\)](https://doi.org/10.1130/2006.2407(03)).

1720
1721
1722 739 **7. Figures**
1723
1724
1725
1726
1727
1728
1729
1730
1731
1732
1733
1734
1735
1736

1737
1738
1739
1740
1741
1742
1743
1744
1745
1746
1747
1748
1749
1750
1751
1752
1753
1754
1755
1756
1757
1758
1759
1760
1761
1762
1763
1764
1765
1766
1767
1768
1769
1770
1771
1772
1773
1774
1775
1776
1777
1778
1779
1780
1781
1782
1783
1784
1785
1786
1787
1788
1789
1790
1791
1792

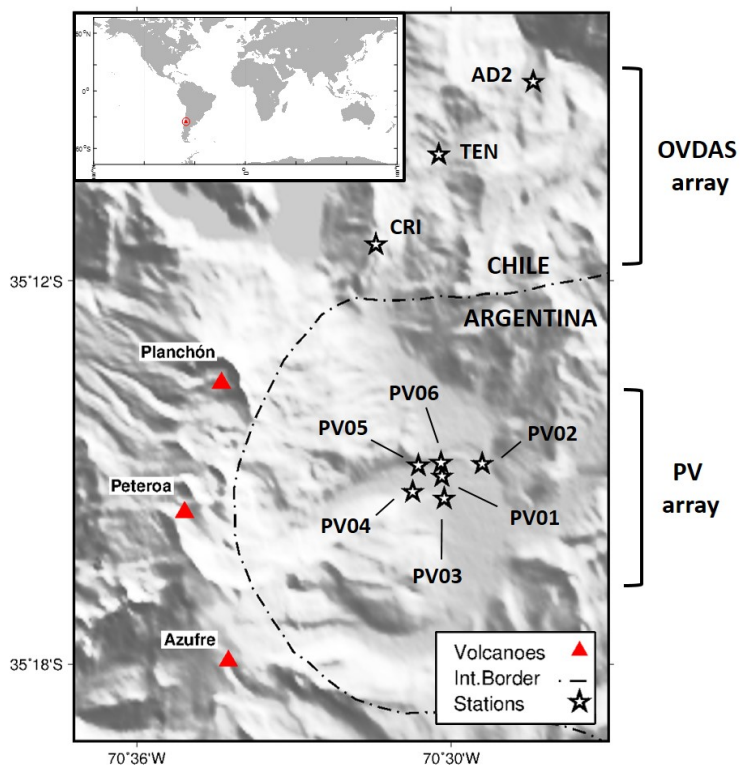


Figure 1: Distribution of the seismic stations used in the present application in relation to the main edifices of the Planchón-Peteroa Volcanic Complex (PPVC).

1793
 1794
 1795
 1796
 1797
 1798
 1799
 1800
 1801
 1802
 1803
 1804
 1805
 1806
 1807
 1808
 1809
 1810
 1811
 1812
 1813
 1814
 1815
 1816
 1817
 1818
 1819
 1820
 1821
 1822
 1823
 1824
 1825
 1826
 1827
 1828
 1829
 1830
 1831
 1832
 1833
 1834
 1835
 1836
 1837
 1838
 1839
 1840
 1841
 1842
 1843
 1844
 1845
 1846
 1847
 1848

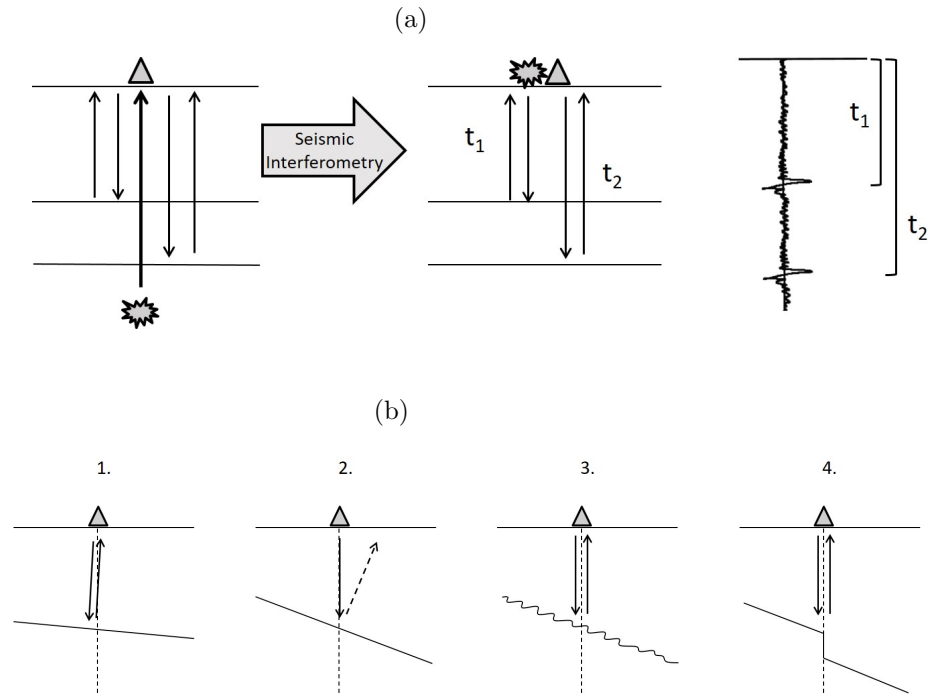


Figure 2: (a) Seismic interferometry by autocorrelation applied to vertically arriving energy in a horizontally layered medium. Parameter t_j represents the two-way travel time between the station at the surface and the reflector j in the subsurface. The autocorrelation allows the retrieval of a seismogram composed of reflected energy released by a virtual source co-located at the position of the station. Each layer is heterogeneous, which is perceived by the arriving energy at times between strong arrivals. For sake of simplicity, we show only vertical-component results with reflector multiples removed. (b) Schematic scenarios in which the applied methodology would (would not) retrieve seismic reflection energy from a subsurface layer. Solid arrows represent seismic energy leaving or arriving at the station, while a dashed arrow indicates seismic energy not arriving at the station. A dashed line shows the vertical as a reference. 1. A sub-horizontal layer; 2. A steep layer; 3. A stair-like steep layer; 4. A steep layer with an abrupt discontinuity along its structure (Nishitsuji et al., 2016).

1849
1850
1851
1852
1853
1854
1855
1856
1857
1858
1859
1860
1861
1862
1863
1864
1865
1866
1867
1868
1869
1870
1871
1872
1873
1874
1875
1876
1877
1878
1879
1880
1881
1882
1883
1884
1885
1886
1887
1888
1889
1890
1891
1892
1893
1894
1895
1896
1897
1898
1899
1900
1901
1902
1903
1904

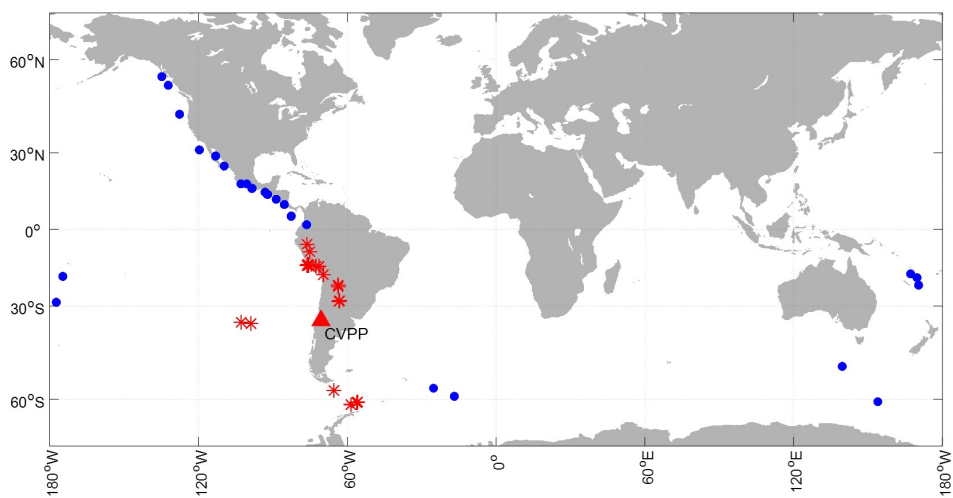


Figure 3: Location of seismic events pre-selected for the application of SIbyA in the area of the PPVC. A triangle indicates the location of the main edifices constituting the PPVC. Stars show the location of events with epicentral distances less than 30° and magnitudes $M_w > 5$. Circles indicate events with epicentral distances greater than 30° and less than 120° , and magnitudes $M_w > 6$.

1905
1906
1907
1908
1909
1910
1911
1912
1913
1914
1915
1916
1917
1918
1919
1920
1921
1922
1923
1924
1925
1926
1927
1928
1929
1930
1931
1932
1933
1934
1935
1936
1937
1938
1939
1940
1941
1942
1943
1944
1945
1946
1947
1948
1949
1950
1951
1952
1953
1954
1955
1956
1957
1958
1959
1960

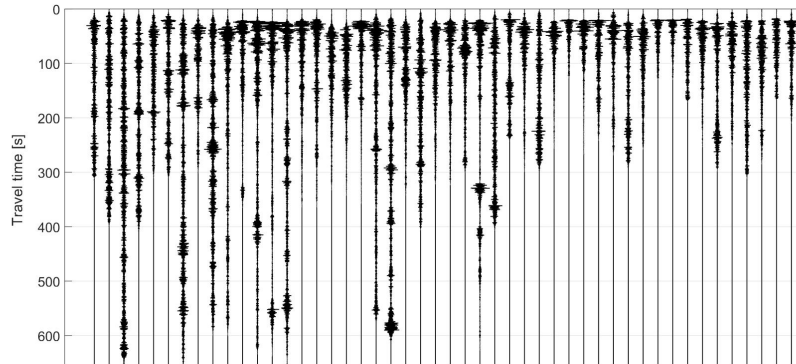


Figure 4: Processing time windows (vertical-component P-wave windows) for each of the events selected for PV04 station for frequencies $[0.8 \ 3]$ Hz. Each window is normalized according to its vertical energy flux. Vertical axis indicates propagation time. Each window is composed of a pre-event time (20 s) and the times between the first P- and S-wave arrival times.

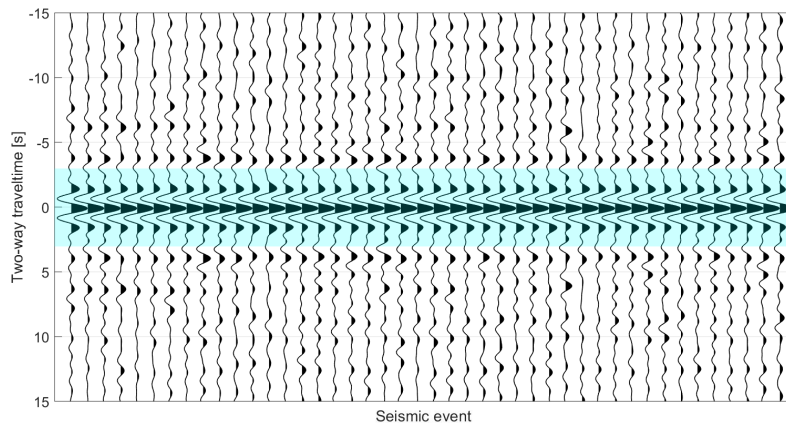
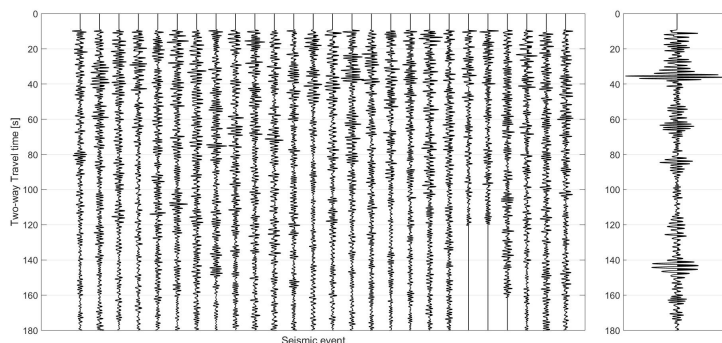


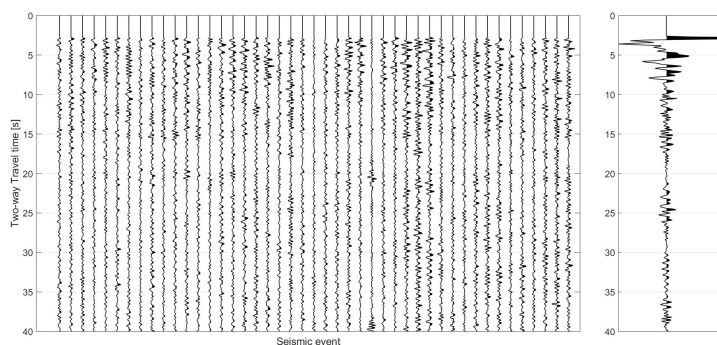
Figure 5: Autocorrelated source time functions (ASTFs) estimated for the vertical component of station AD2 for the frequency range $[0.3 \ 0.8]$ Hz. A highlighted area shows the ASTFs in the autocorrelation panel (for graphical purposes, we only show the first 15 s).

1961
1962
1963
1964
1965
1966
1967
1968
1969
1970
1971
1972
1973
1974
1975
1976
1977
1978
1979
1980
1981
1982
1983
1984
1985
1986
1987
1988
1989
1990
1991
1992
1993
1994
1995
1996
1997
1998
1999
2000
2001
2002
2003
2004
2005
2006
2007
2008
2009
2010
2011
2012
2013
2014
2015
2016

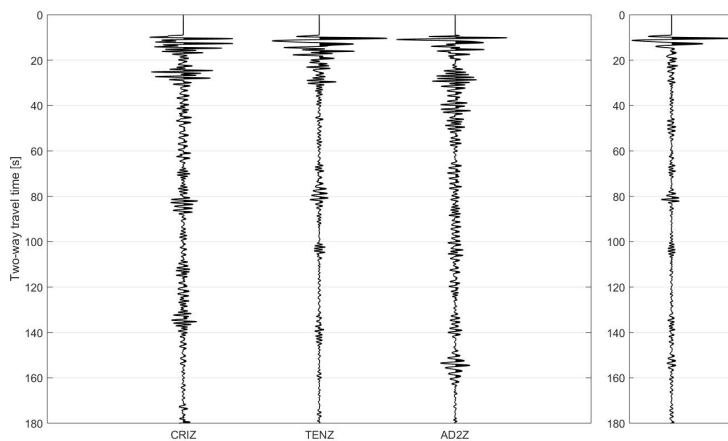
(a) PV05, P wavefield, [0.3 0.8] Hz



(b) CRI, Vertical component, [0.8 3] Hz



(c) Stack OVDAS, Vertical component, [0.3 0.8] Hz



2017
2018
2019
2020
2021
2022
2023
2024
2025
2026
2027
2028
2029
2030
2031
2032
2033
2034
2035
2036
2037
2038
2039
2040
2041
2042
2043
2044
2045
2046
2047
2048
2049
2050
2051
2052
2053
2054
2055
2056
2057
2058
2059
2060
2061
2062
2063
2064
2065
2066
2067
2068
2069
2070
2071
2072

(d) Stack PV, P wavefield, [0.8 3] Hz

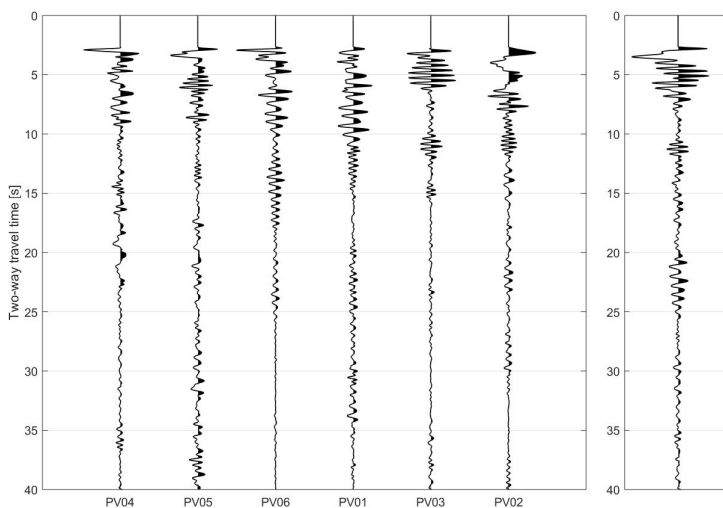


Figure 6: Pre-stacking panels (left) and stacked seismic trace (right) for (a) station PV05 using the P-wavefield data for the frequency range [0.3 0.8] Hz, and (b) station CRI using the vertical-component data for the frequency range [0.8 3] Hz. We also show the individual retrieved reflection traces at each station (left) and their stacked result (right) for (c) the OVDAS array using the vertical-component data for the frequency range [0.3 0.8] Hz, and (d) the PV array using the P-wavefield data for the frequency range [0.8 3] Hz.

2073
2074
2075
2076
2077
2078
2079
2080
2081
2082
2083
2084
2085
2086
2087
2088
2089
2090
2091
2092
2093
2094
2095
2096
2097
2098
2099
2100
2101
2102
2103
2104
2105
2106
2107
2108
2109
2110
2111
2112
2113
2114
2115
2116
2117
2118
2119
2120
2121
2122
2123
2124
2125
2126
2127
2128

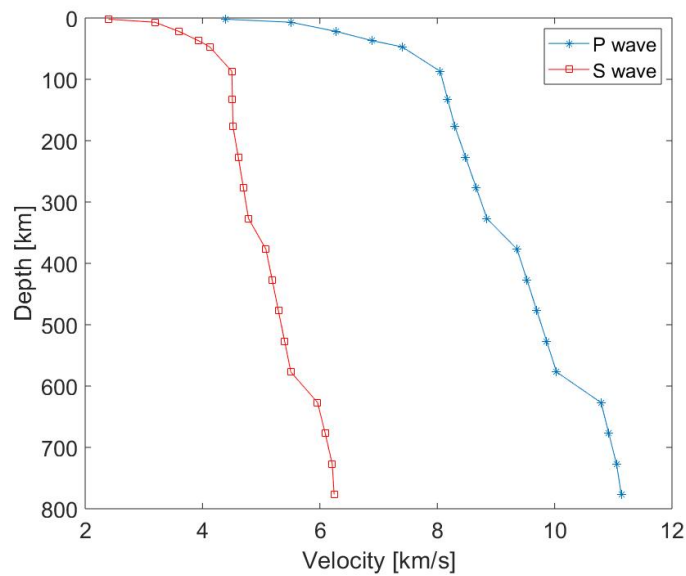


Figure 7: Velocity model used to perform the time-to-depth transformation of the retrieved zero-offset reflection traces.

2129
 2130
 2131
 2132
 2133
 2134
 2135
 2136
 2137
 2138
 2139
 2140
 2141
 2142
 2143
 2144
 2145
 2146
 2147
 2148
 2149
 2150
 2151
 2152
 2153
 2154
 2155
 2156
 2157
 2158
 2159
 2160
 2161
 2162
 2163
 2164
 2165
 2166
 2167
 2168
 2169
 2170
 2171
 2172
 2173
 2174
 2175
 2176
 2177
 2178
 2179
 2180
 2181
 2182
 2183
 2184

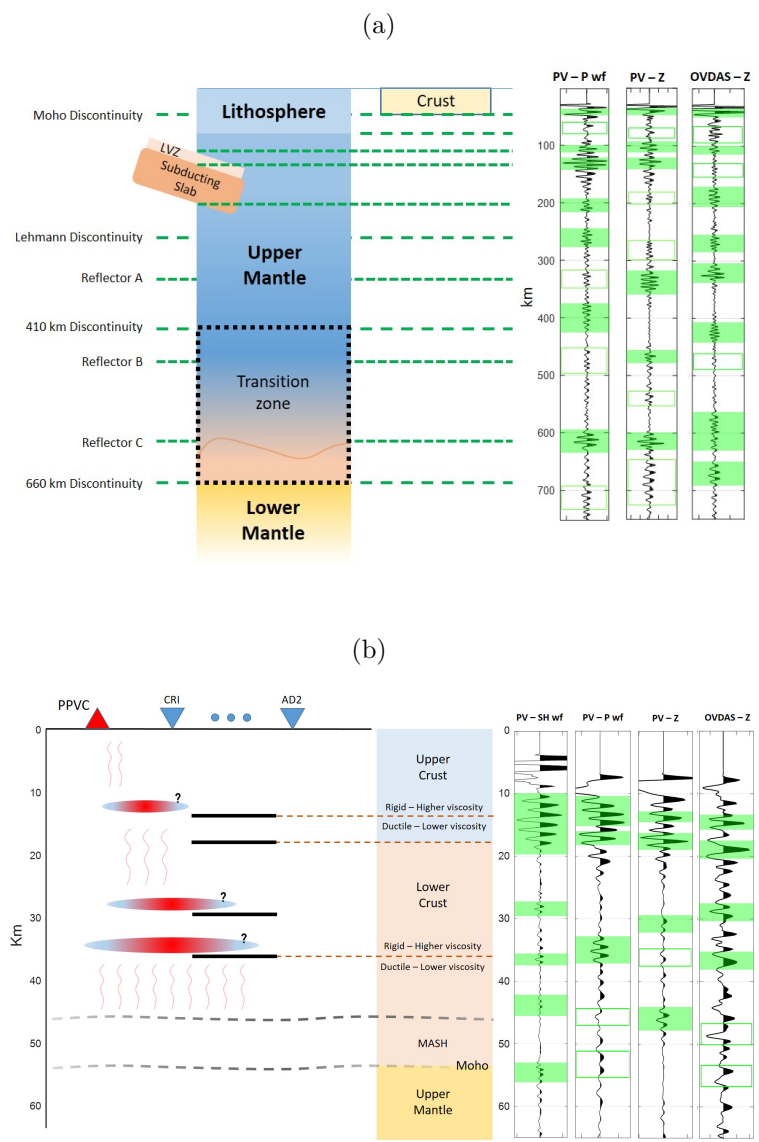


Figure 8: Interpretation of the results for [0.3 0.8] Hz, (b) [0.8 3] Hz. Filled rectangle areas in the seismic results show the local maximum amplitudes, i.e., the interpreted subsurface discontinuities below each array. Empty rectangles indicate a higher uncertainty at the identification of a discontinuity. Vertical axes are in km; the horizontal size of the interpreted features is arbitrary and it does not follow any particular scale. In (b), inverted triangles indicate the longitude of the stations, thick horizontal lines below the stations show the average depth of the reflectors interpreted in the seismic results, and dashed lines are the interpreted discontinuities between the different regions of the crust (based on [Fariás et al. \(2010\)](#) and [Giambiagi et al. \(2012\)](#)). Question marks indicate zones of likely magma storage based on [Jackson et al. \(2018\)](#). MASH = Melting, Assimilation, Storage and Homogenization zone ([Gilbert et al., 2006](#)).

Conflict of Interest and Authorship Conformation Form

Please check the following as appropriate:

- ✓ All authors have participated in (a) conception and design, or analysis and interpretation of the data; (b) drafting the article or revising it critically for important intellectual content; and (c) approval of the final version.
- ✓ This manuscript has not been submitted to, nor is under review at, another journal or other publishing venue.
- ✓ The authors have no affiliation with any organization with a direct or indirect financial interest in the subject matter discussed in the manuscript
- The following authors have affiliations with organizations with direct or indirect financial interest in the subject matter discussed in the manuscript:

Author's name	Affiliation
CASAS, José Augusto	Facultad de Ciencias Astronómicas y Geofísicas, UNLP, CONICET, Argentina
BADI, Gabriela Alejandra	Facultad de Ciencias Astronómicas y Geofísicas, UNLP, Argentina
FRANCO, Luis	Observatorio Vulcanológico de los Andes del Sur, SERNAGEOMIN, Chile
DRAGANOV, Deyan	Department of Geoscience and Engineering, Delft University of Technology, The Netherlands

Author statement:

Casas, José Augusto

Conceptualization, Software, Formal analysis, Writing - Original Draft and Editing

Badi, Gabriela Alejandra

Conceptualization, Writing - Review & Editing

Franco, Luis

Resources

Draganov, Deyan

Conceptualization, Formal analysis, Writing - Review & Editing